Progress In Electromagnetics Research C, Vol. 99, 239–250, 2020

Thermal Analysis of Bearingless Switched Reluctance Motor

Binbin Zhang* **and Zewei He**

Abstract—A bearingless switched reluctance motor (BSRM) has the same body structure as a switched reluctance motor (SRM), but the winding method is different. The accurate analysis of thermal characteristics is especially important for the service life and safety performance of the two motors. According to the initial design parameters, the initial size calculation equations of SRM and BSRM are given, and the ontology design parameters are obtained according to the same design goal. The two-dimensional finite element model is established, and the stator rotor iron loss is analyzed. The distribution characteristics of iron loss of SRM and BSRM are summarized. Secondly, the three-temperature field model of the motor is built, and the reasonable boundary conditions are set. The temperature distribution law of the two motors is analyzed. It is concluded that the BSRM components have lower loss and lower temperature rise under the same design target.

1. INTRODUCTION

The switched reluctance motor (SRM) has no windings and permanent magnets in the rotor, which has many advantages such as simple structure, high mechanical strength, good speed regulation performance, low manufacturing cost, high reliability, flexible control mode, good fault tolerance, and high efficiency. It is suitable for extreme environments such as high temperature and aerospace [1]. The bearingless switched reluctance motor (BSRM) has the same structure on the stator of SRM and the magnetic bearing stator, and introduces the magnetic bearing technology into the SRM, so that the motor has both rotation and suspension functions, which has great prospects in the field of high-speed motors. The use rate of BSRM motors in various fields is increasing year by year, but the problem of heating is becoming more and more prominent, and has begun to be included in research priorities [2–5].

Due to the good characteristics of BSRM, it is often used in special operating condition; correspondingly, it is particularly important to analyze the temperature characteristics of the motor. However, it is worth noting that there are currently few studies on loss calculation and temperature analysis for BSRM. With the rapid development of finite element software and the continuous verification of empirical formulas, the calculation of heat dissipation coefficient and thermal resistance can approximate the temperature distribution of the motor, but most of the researches are still in stage of simulation, and the heat transfer theory does not deepen the study. In [6], the iron loss characteristics of SRM were studied, and the Stanmeet method was used to study the iron loss. Finally, the main parameters affecting the iron loss of the motor were analyzed. Ref. [7] introduced the motor optimization design based on the magneto-thermal coupling method. Ref. [8] proposed a fast and accurate analysis method to analyze the loss and efficiency of a four-phase 16/12-pole SRM under different working conditions. Ref. [9] proposed a calculation method for the copper loss of SRM high-efficiency windings, which has obvious advantages in optimizing the winding configuration. Refs. [10–12] analyzed the temperature rise caused by iron loss and copper loss in SRM by two-dimensional and three-dimensional finite element method. In [13], the iron loss characteristics of BSRM are analyzed, and a

Received 13 November 2019, Accepted 12 January 2020, Scheduled 11 February 2020

* Corresponding author: Binbin Zhang (zhangbin416@qq.com).
The authors are with the State Grid LinFenShi YaoDuQu Power Supply Company, Linfen, Shanxi 041000, China.

new calculation method of iron loss is proposed. The main design parameters affecting iron loss are given. Ref. [14] introduced the temperature field distribution law of a switched reluctance motor under different operating conditions. Refs. [15] and [16] respectively introduced the temperature field analysis process of SRM and BSRM, and analyzed the motor temperature distribution under rated conditions.

In this paper, a three-phase 12/8 SRM and a three-phase 12/8 BSRM are designed. The finite element analysis of the magnetic density of the typical position of the motor is carried out, and the distribution law of iron loss of each component is calculated. Secondly, the loss is introduced into the heat as a heat source. In the model, the temperature distribution characteristics of BSRM and SRM motors are analyzed, which provide a reference for BSRM temperature prediction, reliability analysis, and electromagnetic design under the corresponding working conditions.

2. ONTOLOGY DESIGN OF SRM AND BSRM

The design of the motor is closely related to the establishment of the body size, so the derivation of the body size calculation formula is particularly important. The body size expression of a normal SRM:

$$DL = \frac{60\mu_0 Z_s P_2}{(1-k_{\mathrm{m}})\, cmn\pi\alpha_s Z_r B_\delta^2 k_m \delta} \tag{1}$$

where c — Number of winding series and parallel branches; Z_r — Number of rotor teeth; μ_0 — Permeability coefficient of air; D — Inner diameter of stator; L — Stack length; m — Phase; n — Rotating speed; α_s — Pole arc coefficient of stator; Z_s — Number of stator teeth; k_m — Core magnetic pressure drop coefficient; δ — Air gap length; B_δ — Magnetic density of air gap; P_2 — Output Power.

Since the BSRM structure is similar to the SRM motor structure, the BSRM can refer to the SRM body design method. However, the BSRM winding connection method and the control method are quite different from the ordinary SRM. It is necessary to redetermine the calculation formula of the BSRM body size, as shown in Equation (2).

$$D_{\mathrm{r}} l = \frac{90 P_{\mathrm{em}} \mu_0}{\pi mnk_l k_{\mathrm{m}} \delta\, (B_m^2 + B_s^2)} \tag{2}$$

where D_r — Rotor outer diameter; P_{em} — Electromagnetic power; k_l — Permeability ratio coefficient; B_m — The air gap magnetic density maximum formed by the torque component iTa when the rotor teeth are aligned with the stator teeth; B_s — The air gap magnetic density maximum formed by the suspension component iSa when the rotor teeth are aligned with the stator teeth.

Comparing Equation (1) with Equation (2), the difference between the size determinations of the two motor bodies is that the air gap magnetic density maximum is different in expression, wherein the air gap magnetic field of the BSRM is composed of both the torque component and levitation component. The generated magnetic fields are superimposed. It can be seen from Equation (2) that the values of B_m and B_s not only affect the calculation of the size of the body, but also have an influence on the determination of the number of winding turns.

The BSRM has a suspension function, and the derivation of the suspension force calculation formula is also crucial. The motor is a double salient pole structure. The permeance changes periodically with the rotor position angle, and its instantaneous radial levitation force also changes periodically with the rotor position angle. When the load is constant, it is more meaningful to derive the average levitation force in one cycle, as shown in Equation (3):

$$F_{\mathrm{avg}} = \frac{12}{\pi} \int_{-\frac{\pi}{12}}^{0} F_a d\theta = \frac{24\sqrt{2}\mu_0 lr N_{\mathrm{s}}^2}{\pi k_{\mathrm{m}} \delta} \left[\frac{\pi^2}{288\delta} + \frac{1}{3r} - \frac{4\delta}{cr^2} \mathrm{In}\left(1 + \frac{cr}{3\delta}\right) \right] I_{\mathrm{pm}} I_{\mathrm{ps}} \tag{3}$$

where c — constant; r — Rotor radius; δ — Air gap length; I_{pm} — Peak value of torque component; I_{ps} — Peak value of suspending component.

Figure 1 shows the basic parameters of the motor.

The design goals and initial parameters of the motor are shown in Table 1. The main parameters of the SRM and BSRM prototypes can be given according to the relevant initial parameters in Table 1, as shown in Table 2.

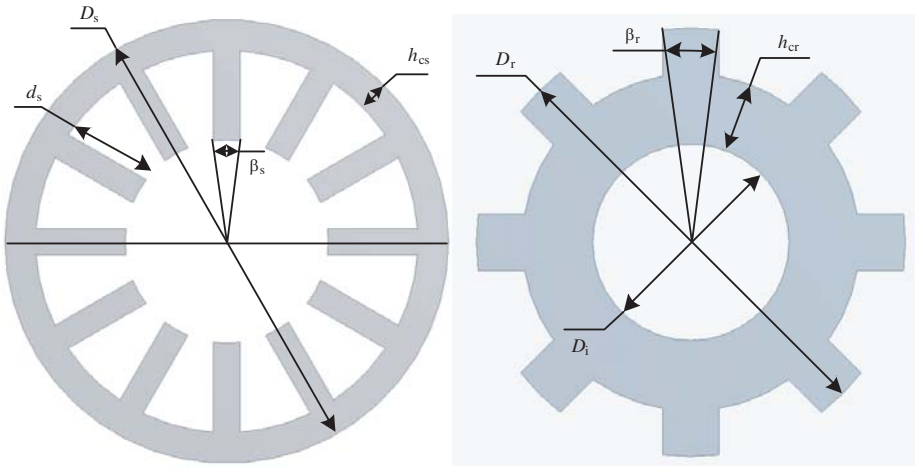

Figure 1. The basic structural dimensions of the stator and rotor.

Table 1. Design objects and preliminary parameters.

P	U	n	η	F	δ	B_m, B_s
1.1 KW	220 V	6000 r/min	$> 75\%$	180 N	0.25 mm	0.8 T
k_m	k'	J	μ_0	k_f	k_l	β_s, β_r
1.16	1.4	5 A/mm^2	$4\pi\times10^{-7}$	1.4	0.84	15°

Table 2. Dimensions of SRM and BSRM.

Parameter	SRM	BSRM
D_s/mm	96	130
D_r/mm	51	59
D_i/mm	25.3	27
L/mm	56.5	70
β_s/(°)	15	15
β_r/(°)	15	15
h_{cs}	4.5	9
h_{cr}	5	9.7
N_s/turns	42	33
F_{avg}/N	-	189

3. LOSS CHARACTERISTICS OF SRM AND BSRM

Since BSRM and SRM core structures are identical, the analysis of the BSRM iron loss can be based on the relevant method of SRM iron loss analysis. The motor is a double salient pole structure. The magnetic field changes on the stator and rotor are complicated. It is not a simple alternating magnetization, and there is also a rotating magnetization. When the magnetic density generated inside the motor is an arbitrary waveform, the iron loss calculation expression is:

$$P_{\mathrm{FE}} = k_{\mathrm{h}} f B_m^a + \frac{\sigma\delta^2}{12\rho T}\int_0^T \left(\frac{dB_{\mathrm{r}}(t)}{dt}\right)^2 + \left(\frac{dB_{\mathrm{t}}(t)}{dt}\right)^2 dt + \frac{\sqrt{\sigma G V_0 S}}{\rho T}\int_0^T \left|\frac{dB_{\mathrm{r}}(t)}{dt}\right|^{1.5} + \left|\frac{dB_{\mathrm{t}}(t)}{dt}\right|^{1.5} dt \quad (4)$$

where k_h, a — Hysteresis loss coefficient obtained by fitting PB curve; f — Fundamental frequency; B_m — Maximum value of magnetic density; σ — Core material conductivity; δ — Core material thickness; ρ — Core material density; B_r — Radial magnetic density component; B_t — Tangential magnetic density component; G, V_0 — Material correlation coefficient; S — Core material cross-sectional area.

When the magnetic density waveform is sinusoidal, Equation (4) can be rewritten as:

$$P_\mathrm{FE} = k_\mathrm{h} f B_m^a + k_\mathrm{c} f^2 B_m^2 + k_\mathrm{e} f^{1.5} B_m^{1.5} \tag{5}$$

where k_c — Eddy current loss factor; k_e — Additional loss factor.

It can be seen from Equation (5) that the calculation of iron loss is determined by various loss factors, frequencies and magnetic density of the material. When the motor runs stably, the frequency is constant at this time. Therefore, the iron loss value can be calculated by simply obtaining the loss coefficient and the magnetic density amplitude of the core material.

In practice, the motor is often in a high-speed operation state, and the magnetic density in the iron core is not distributed according to the standard sinusoidal waveform. Therefore, in order to correctly calculate the iron loss, it is necessary to study the magnetic density waveform at different places on the stator, perform Fourier decomposition calculation, and then add the iron loss generated by each harmonic to obtain the iron loss of the motor. However, it is impossible to analyze the magnetic-density waveform at each position on the stator, so a simple equivalent and correct method must be adopted. In this paper, the typical positions of different parts of the stator core are taken, and time-step finite element analysis is carried out, as shown in Fig. 2. Point 1 is located in the middle of the stator yoke, point 2 in the stator pole, point 3 at the pole tip of the stator, point 4 at the pole tip of the rotor, point 5 located in the rotor teeth, and point 6 located in the rotor yoke.

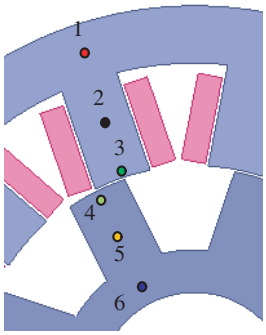

Figure 2. Select point distribution.

The variation of the radial component B_r and the tangential component B_t of the magnetic density of each point in a change period is calculated by ANSOFT, as shown in Fig. 3.

As can be seen from Fig. 3, the stator pole tip has a large magnetic density amplitude because the magnetic field lines pass through the air gap from the stator pole tip and flow through the rotor to form a closed path. At the same time, only the phase difference between the radial magnetic density component and the tangential magnetic density component at points 2 and 5 is approximately 0° or 180°, and the magnetic field direction is reversed. Therefore, there is a rotating magnetic field and an alternating magnetic field in the stator pole tip and the yoke portion, and only an alternating magnetic field exists in the stator pole. There is a rotating magnetic field and an alternating magnetic field in the pole tip and the yoke of the rotor, and only an alternating magnetic field exists in the rotor pole. Therefore, when there is an arbitrary magnetic field waveform in the core, whether it is an alternating magnetic field or a rotating magnetic field, or a combined magnetic field that interacts with the two, it can be decomposed into two orthogonal alternating magnetic fields for analysis.

Table 3 gives the performance parameters of the stator and rotor core material, and the additional loss of the material is negligible. Assuming that both the magnetic density components B_r and B_t show a sinusoidal change law, and the magnitudes of the magnetic losses at the rated speed can be calculated by substituting their amplitudes into Equation (4).

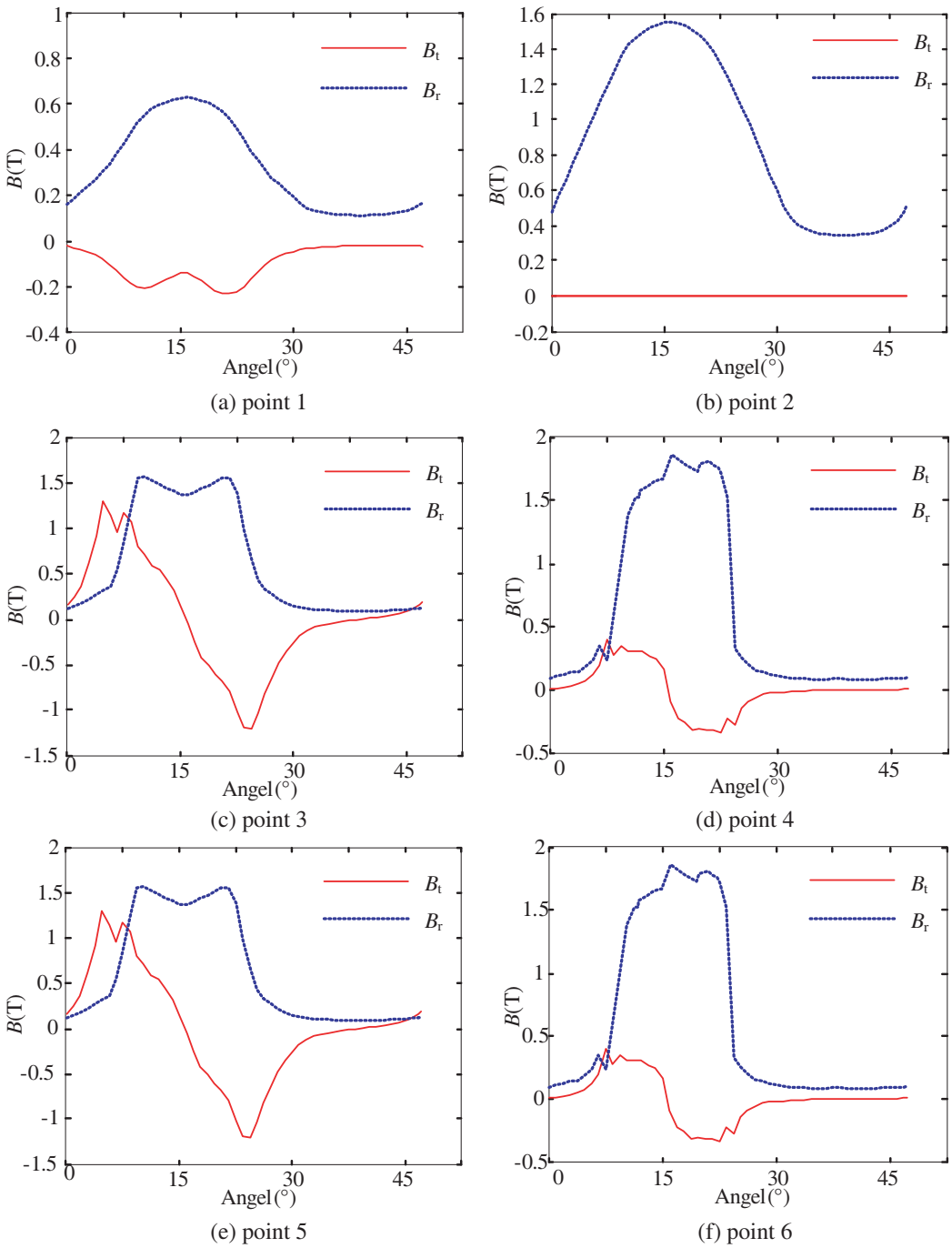

Figure 3. Magnetic density curve at each position.

Figures 4 and 5 show the distribution of stator-rock loss density at different rotor positions of BSRM and SRM, respectively. It can be seen from the figure that the iron loss density distribution of the rotor is different at different positions. The iron loss of the two motors is concentrated on the stator pole teeth and is less in the yoke portion. The distribution of iron loss at the tip of the fixed rotor is denser than that in the tooth. This is due to the double salient pole structure of the motor, which rotates according to the principle of minimum reluctance, and the magnetic lines of force are dense at the tip position. From the calculation of the overall iron loss of the motor, the BSRM stator

Table 3. Characteristics of stator and rotor material (DW360_50).

Parameter	Value
density δ (kg/m^3)	7650
Thickness d (mm)	0.35
Lamination rate	0.94
k_h	176.84
k_c	0.87
k_e	0

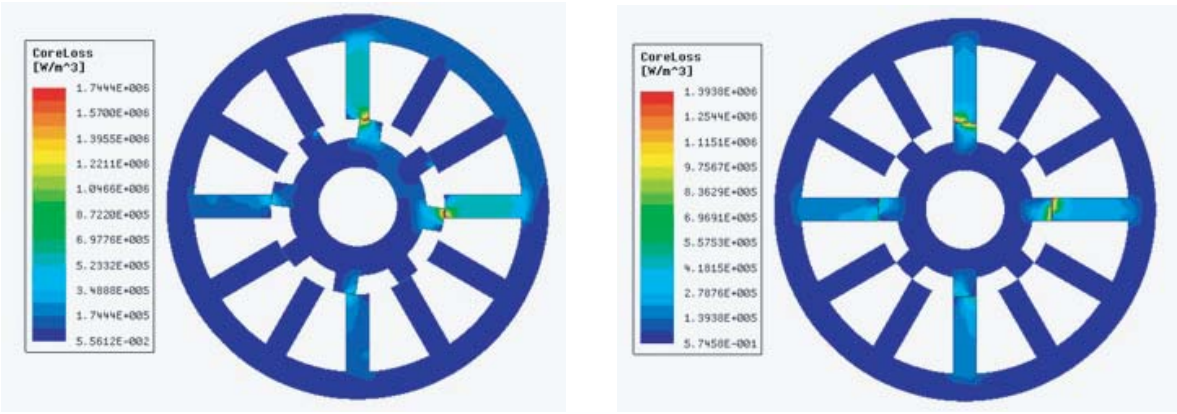

(a) Middle position (b) Alignment position

Figure 4. Distribution of iron loss density at different positions of BSRM.

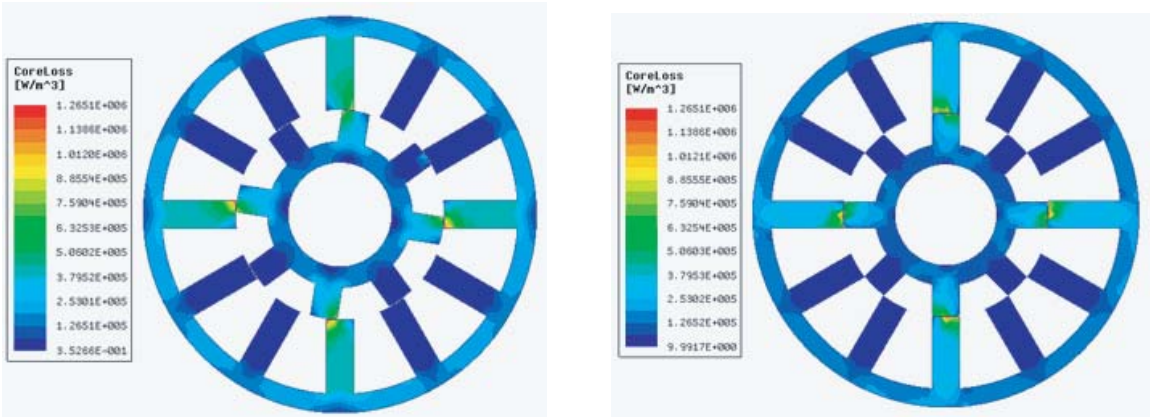

(a) Middle position (b) Alignment position

Figure 5. Distribution of iron loss density at different positions of SRM.

iron loss is 130.12 W, of which the eddy current loss is 119.24 W, accounting for 91.3%; the hysteresis loss is 10.88 W, accounting for 8.7%. The rotor iron loss is 61.53 W, wherein the eddy current loss is 58.02 W, accounting for 94.3%; the hysteresis loss is 3.51 W, accounting for 5.7%. At the same time, it can be obtained from Fig. 4 and Fig. 5 that under the same design goal, the SRM iron loss density distribution is larger than the BSRM iron loss density, and the BSRM iron loss value is lower.

4. TEMPERATURE ANALYSIS OF SRM AND BSRM

4.1. Construction of Thermal Model

In this paper, the unidirectional coupling method is adopted, and the influence of temperature change on the motor parameters is not considered. The main analysis process is to determine the initial structural parameters of the SRM based on the motor design criteria. 2D models and 3D thermal analysis models are built using Ansys finite element analysis software. The electromagnetic performance of motor is analyzed in the solver to obtain the loss distribution of motor. Then the loss is introduced into the workbench 3D thermal model as a heat source for transient thermal analysis to obtain the temperature distribution of each component of the motor. Since the gas flow and heat transfer in the motor is a complicated process, in order to simplify the model, the following reasonable assumptions are given:

1) The thermal coefficients of the material do not change with temperature, and only the average effect of temperature is considered.
2) The ambient temperature of the motor remains unchanged, and the initial temperature of the motor is the same as the ambient temperature.
3) The heat dissipation coefficient is an average value.
4) The motor adopts distributed winding, and the winding is replaced by a rectangular parallelepiped. All the insulation in the stator slot is insulated from the slot, and the winding copper wire is equivalent to a heat conductor.
5) Use the thermal conductivity of the stationary gas to equal the thermal conductivity of the air rotating in the air gap.
6) Ignoring the influence of the pole arc on the temperature distribution, the axial temperature gradient of the motor is considered to be zero.

Based on the above assumptions, when the motor is running transiently, the 3D heat conduction equation is as shown in Equation (6):

$$\begin{cases} \dfrac{\partial}{\partial x}\left(k_x \dfrac{\partial T}{\partial x}\right) + \dfrac{\partial}{\partial y}\left(k_y \dfrac{\partial T}{\partial y}\right) + \dfrac{\partial}{\partial z}\left(k_z \dfrac{\partial T}{\partial z}\right) = c\gamma \dfrac{\partial T}{\partial y}\tau - q \\ -k\dfrac{\partial T}{\partial n}\,|_{S_1} = 0 \\ -k\dfrac{\partial T}{\partial n}\,|_{S_2} = \alpha\,(T - T_f) \end{cases} \tag{6}$$

where k_x, k_y, k_z — The thermal conductivities of the motor material in the x, y, and z directions; τ — Running time(s); c — Specific heat capacity; γ — Material density; q — The sum of the density of each heat source; T — Solution temperature of the object; α — Heat dissipation coefficient of the surface; T_f — Temperature of fluid around the heat surface.

The winding of the machine is a heterogeneous structure consisting of insulation, air, and copper wires. These materials have totally different thermal behaviors. It is a common practice to consider an equivalent thermal conductivity coefficient for the winding which can be obtained by various methods (analytical approach, FEM, experiments). In this model, conductors having the same temperature are lumped together to make a copper layer. Layers of copper that have roughly equal temperature are expected to have a similar distance from the stator laminations. The copper layer thickness is assumed equal to that of the bare conductor diameter, and the number of layers (with the spacing between them) is set so that the entire copper area is equal to that of the actual machine. This winding model helps to visualize the slot fill and show where the hot spot is likely to be.

Based on the above analysis, an equivalent 3D model is established as shown in Fig. 6. At the same time, the thermal conductivity of the various components can be determined. Since the axial thermal conductivity of the copper strand and the stator core lamination is relatively high and the radial difference is large, the material parameter is designed as shown in Table 4.

When the motor is running, the air gap between the stator and rotor changes momentarily, and the heat dissipation process is complicated. It is difficult to establish an accurate model. Therefore, in order

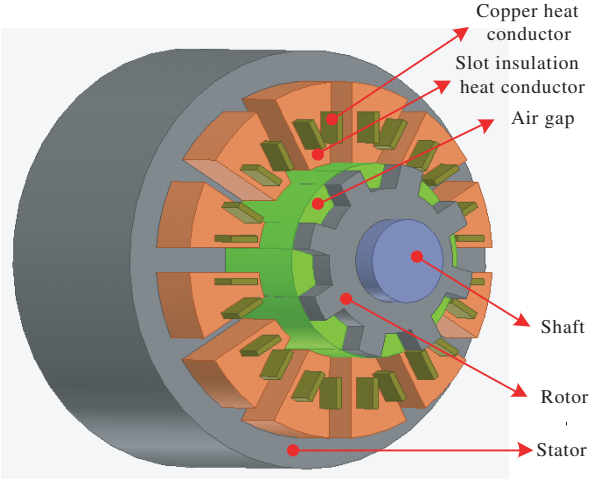

Figure 6. 3-D thermal model of motor.

Table 4. Dimensions of material.

Part	material	density (kg/m^3)	Specific heat capacity ($J/kg \cdot K$)	Thermal Conductivity ($W/(m \cdot K)$)
Stator and rotor	DW470	7800	450	70
slot insulation	Composite material	1.2	1340	0.3
Winding	Copper	8900	390	386
Air gap	Air	1.29	1004	0.023
Shaft	Aluminum	2700	903	204

to simplify the calculation, the designer draws lessons from practice and uses the empirical formula to derive the surface heat dissipation coefficient of each component under natural cooling conditions.

1) Heat dissipation coefficient of the outer surface of the stator yoke:

$$\alpha_1 = 40\,\mathrm{W/m^2 \cdot {}^\circ C} \tag{7}$$

2) Stator end surface heat dissipation coefficient:

$$\alpha_2 = \frac{1 + 0.04v}{0.045} \tag{8}$$

where v — Rotor line speed (m/s).

3) Rotor end surface heat dissipation coefficient:

$$\alpha_3 = 28\left(1 + \sqrt{0.45v}\right) \tag{9}$$

4.2. Temperature Analysis of Motor

According to the above analysis, the boundary conditions are applied to the 3-D thermal model to solve the temperature field distribution of the stator and rotor when the BSRM is rated under natural air-cooling conditions, as shown in Fig. 7. Fig. 8 shows the temperature profile of various components of the motor.

As shown in Fig. 7(a), the stator temperature is concentrated on the stator teeth, and the temperature is relatively large with respect to the stator yoke. This is because the stator yoke has

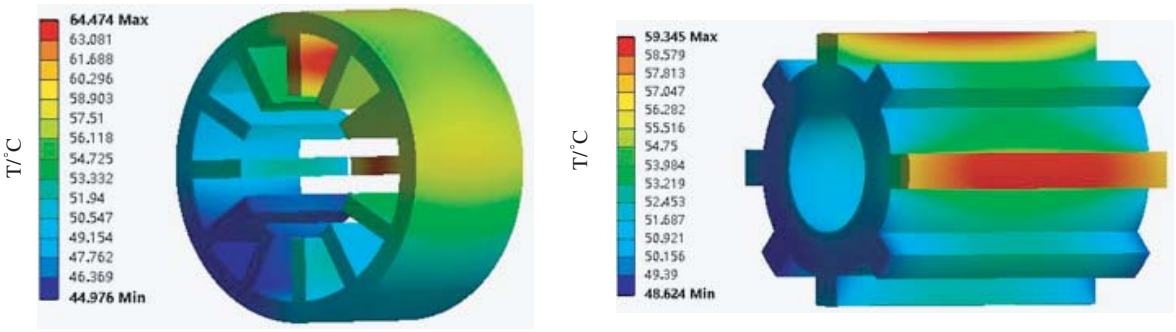

(a) stator (b) rotor

Figure 7. Temperature distribution in stator and rotor of BSRM.

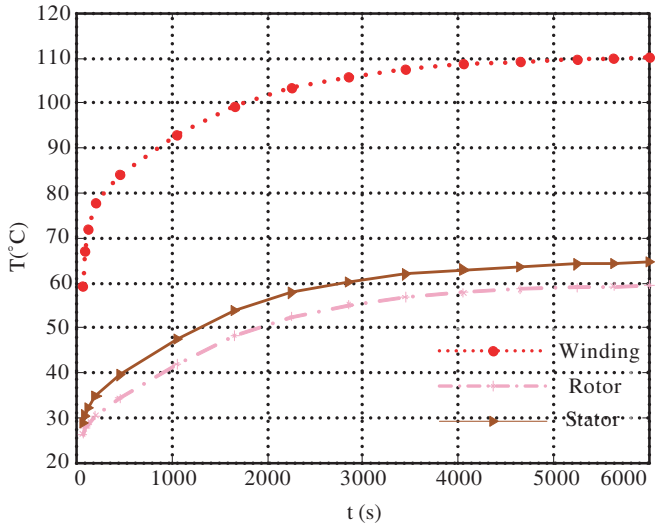

Figure 8. Temperature curve of each component of BSRM.

a small loss, is close to the external environment, and has a large heat dissipation area and good heat dissipation conditions. The windings of the stator teeth are wound, and the windings generate heat seriously. A part of the heat is also transmitted to the stator. As can be seen from Fig. 7(b), the temperature on the rotor side is also concentrated at the rotor teeth, and the temperature is relatively large with respect to the rotor yoke. The highest temperature is distributed in the middle of the tooth axial direction, and the temperature on both sides is low. This is due to the heat transfer between the stator and rotor through the air gap. The heat dissipation condition is poor, and the rotor can dissipate a part of the heat through the rotating shaft connected to the rotor. The rotor end face can also dissipate heat by convection, and the iron loss of the fixed rotor is mainly distributed in the tooth portion. The temperature rise was higher.

It can be seen from Fig. 8 that the temperature rises faster in the first 30 minutes, because the motor temperature in the initial operation is not much different from the external ambient temperature, and the heat generated by the motor loss and external space is less. Between 30 and 50 minutes, the temperature difference between the inner motor and the external space gradually becomes larger; the motor starts to radiate outward; and the temperature gradually increases. After 50 minutes, the heat dissipation of each component and the heat generation reach equilibrium, and the temperature tends to reach a stable state, which basically does not change. At this time, the stator tooth temperature is about 65°C; the rotor tooth tip temperature is about 59°C; and the winding temperature is about 110°C. The steady state temperature of the winding is the highest. This is because the stator winding

is the main heat source. During operation, the winding generates a large copper loss through a large current, which generates a large amount of heat, and the winding does not directly contact the air gap and the stator. A composite insulating material having a small thermal conductivity is provided, and the heat dissipation condition is poor.

Figure 9 is a stator rotor temperature distribution when the SRM is in a steady state under natural air-cooling conditions, and Fig. 10 is a temperature variation curve of each component of the SRM. It can be seen from Figs. 9 and 10 that the temperature distribution law of the SRM stator and rotor is basically the same as that of the BSRM, and the average winding temperature > the average stator temperature > the average rotor temperature.

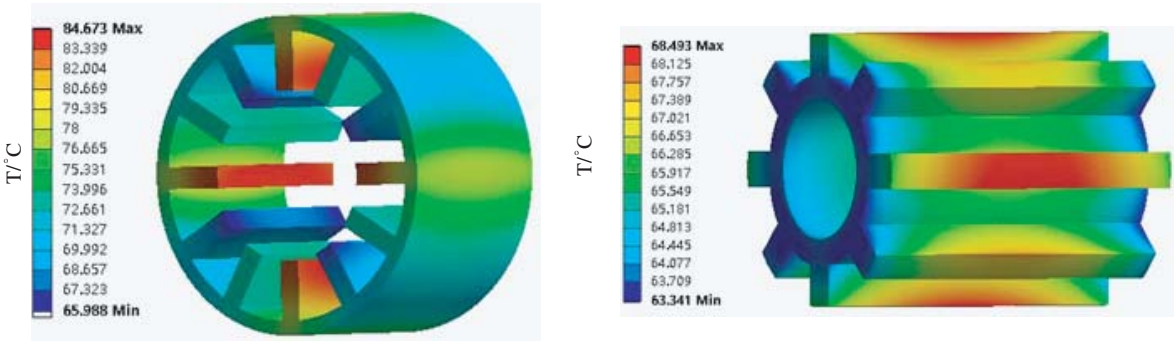

(a) stator (b) rotor

Figure 9. Temperature curve of each component of SRM.

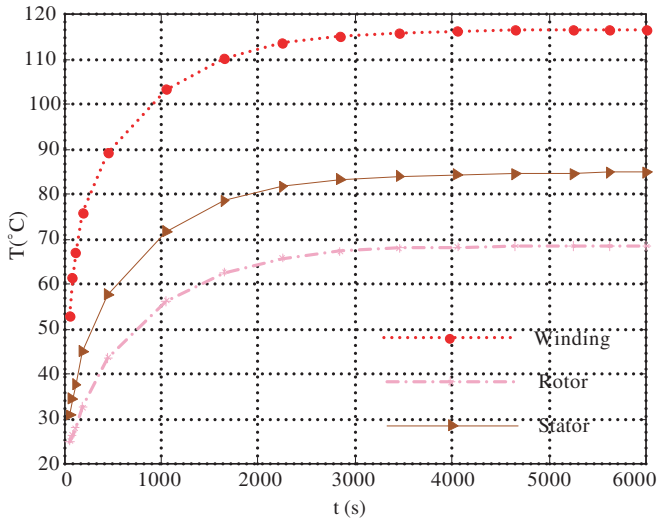

Figure 10. Temperature change curves of stator and rotor of SRM.

Figure 11 shows temperature comparison curves of the components of SRM and BSRM. It can be seen from the figure that the stator, rotor, and winding change laws are basically the same, but the temperature at the steady state is not the same. The BSRM stator steady-state temperature is about 64°C, which is 20°C lower than the SRM; the BSRM rotor steady-state temperature is about 59°C, which is 10°C lower than the SRM; the BSRM winding steady-state temperature is about 110°C, which is 8°C lower than the SRM. Therefore, under natural air-cooling conditions, under the same design goals and heat dissipation conditions, the steady-state temperature of each component of the BSRM is lower than the steady-state temperature of the SRM components, indicating that the BSRM heat generation rate is less than SRM, and the BSRM loss is lower.

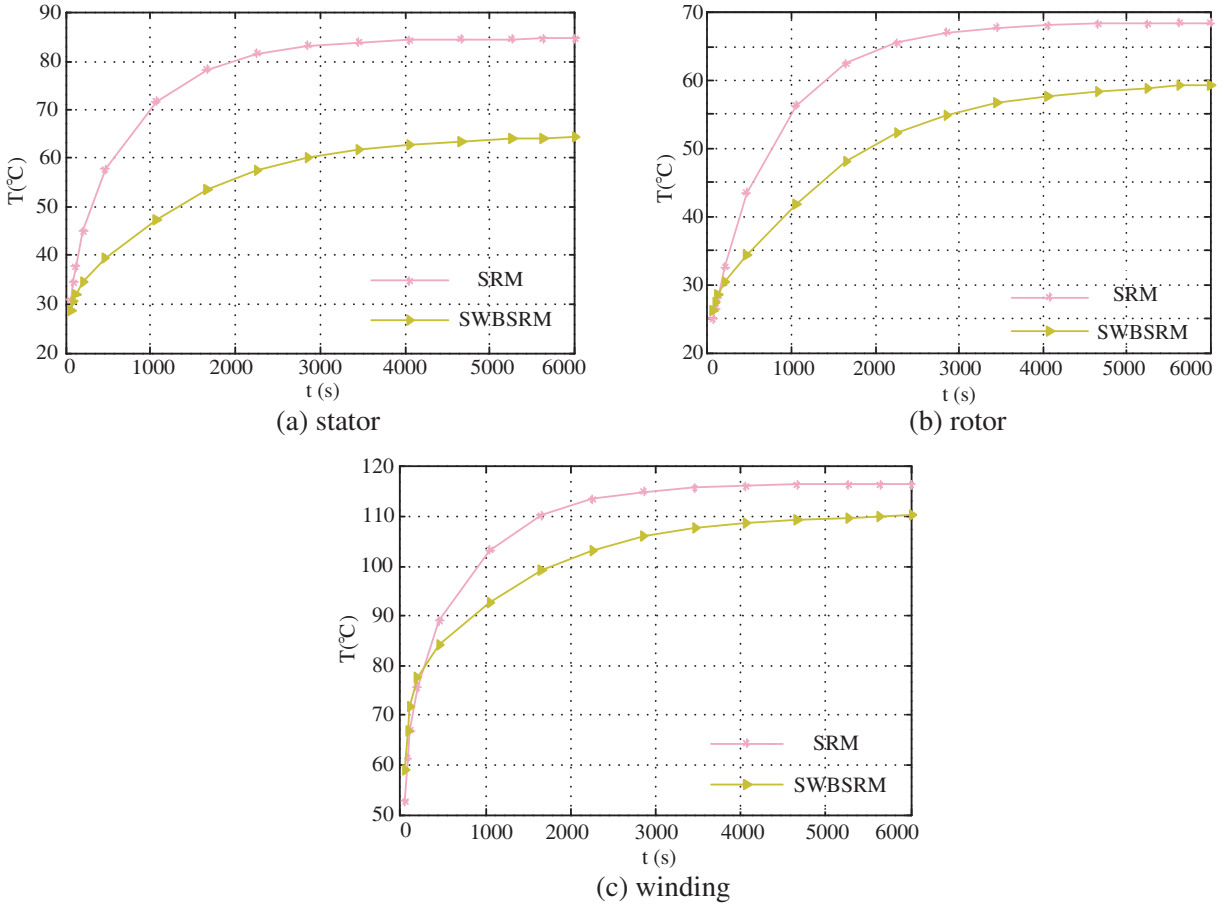

Figure 11. Temperature comparison curve of components between SRM and BSRM.

5. CONCLUSION

The main dimensions design equations of SRM and BSRM are introduced in this paper. The main design parameters of the two motors under the same design target are given. The magnetic density variation of the typical position of the stator and rotor is analyzed, and the iron loss distributions of SRM and BSRM are analyzed by FEA. The results are verified, and the results show that the BSRM loss is lower, and the efficiency is higher at the same speed.

On the basis of the loss analysis, the temperature field of SRM and BSRM under natural air-cooling conditions is analyzed by magnetic-thermal unidirectional coupling method to obtain the temperature distribution of the main components of the motor. The results show that the temperature of each component of BSRM is lower than SRM when it reaches steady state, which is more suitable for high speed environment. The accurate modeling of the temperature field of the switched reluctance motor provides a theoretical reference for the motor optimization design. At the same time, it is necessary to take certain measures to improve the temperature grade of the material and design the corresponding cooling method to reduce the overall temperature of the motor. It has reference significance for the application of the motor in different environments.

REFERENCES

1. Liaw, C. M., K. W. Hu, J. C. Wang, et al., "Development and operation control of a switched-reluctance motor driven flywheel," *IEEE Transactions on Power Electronics*, Vol. PP, No. 99, 1–1, 2018.

2. Sotelo, G. G., L. G. B. Rolim, A. C. Ferreira, et al., "High-speed flywheel system with switched reluctance motor/generator," *IEEE Industry Applications Society Conference, V Induscon*, Vol. 1, IEEE, 2002.
3. Inamura, S., T. Sakai, and K. Sawa, "A temperature rise analysis of switched reluctance motor due to the core and copper loss by FEM," *IEEE Transactions on Magnetics*, Vol. 39, No. 3, 1554–1557, 2003.
4. Castano, S. M., B. Bilgin, J. Lin, et al., "Radial forces and vibration analysis in an external-rotor switched reluctance machine," *IET Electric Power Applications*, Vol. 11, No. 2, 252–259, 2017.
5. Materu, P. N. and R. Krishnan, "Estimation of switched reluctance motor losses," *IEEE Transactions on Industry Applications*, Vol. 28, No. 3, 668–679, 1992.
6. Chen, H., Y. Xu, and H. C. Iu, "Analysis of temperature distribution in power converter for switched reluctance motor drive," *IEEE Transactions on Magnetics*, Vol. 48, No. 2, 991–994, 2012.
7. Sun, H., J. Gao, Y. Dong, et al., "Analysis of temperature field in switched reluctance motor based on finite-element," *Proceedings of the 11th International Conference on Electrical Machines and Systems*, Vol. 2, 597–601, 2008.
8. Boivie, J., "Iron loss model and measurements of the losses in a switched reluctance motor," *1993 Sixth International Conference on Electrical Machines and Drives. IET*, 219–222, 1993.
9. Liu, C., X. Y. Zhu, Y. Du, et al, "Design and performance analysis of magnetic field modulated flux-switching permanent magnet machine based on electrical-thermal bi-directional coupling design method," *Proceedings of the CSEE*, Vol. 37, No. 21, 6237–6245, 2017.
10. Yu, Q., B. Bilgin, and A. Emadi, "Loss and efficiency analysis of switched reluctance machines using a new calculation method," *IEEE Transactions on Industrial Electronics*, Vol. 62, No. 5, 3072–3080, 2015.
11. Yang, Y., B. Bilgin, M. Kasprzak, et al., "Thermal management of electric machines," *IET Electrical Systems in Transportation*, Vol. 7, No. 2, 104–116, 2016.
12. Eit, M. A., P. Dular, F. Bouillault, et al., "Perturbation finite element method for efficient copper losses calculation in switched reluctance machines," *IEEE Transactions on Magnetics*, Vol. 53, No. 6, 1–4, 2017.
13. Li, G. J., J. Ojeda, E. Hoang, et al., "Comparative studies between classical and mutually coupled switched reluctance motors using thermal-electromagnetic analysis for driving cycles," *IEEE Transactions on Magnetics*, Vol. 47, No. 4, 839–847, 2011.
14. Sun, Y., B. Zhang, Y. Yuan, and F. Yang, "Thermal characteristics of switched reluctance motor under different working conditions," *Progress In Electromagnetics Research M*, Vol. 74, 11–23, 2018.
15. Liu, J., X. Zhang, H. Wang, et al., "Iron loss characteristic for the novel bearingless switched reluctance motor," *2013 International Conference on Electrical Machines and Systems (ICEMS)*, 586–591, 2013.
16. Arbab, N., W. Wang, C. Lin, et al., "Thermal modeling and analysis of a double-stator switched reluctance motor," *IEEE Transactions on Energy Conversion*, Vol. 30, No. 3, 1209–1217, 2015.